Predicting the thickness of sand strata in a sand-shale interbed reservoir based on seismic facies analysis

Huilin Li[1], Rui Gao[1,2,*] and Yanghua Wang [iD][3]

[1] School of Earth Sciences and Engineering, Sun Yat-Sen University, Guangzhou 510275, China
[2] Institute of Geology, Chinese Academy of Geological Sciences, Beijing 100037, China
[3] Centre for Reservoir Geophysics, Resource Geophysics Academy, Imperial College London, South Kensington, London SW7 2BP, UK

*Corresponding author: Rui Gao. E-mail: gaorui66@mail.sysu.edu.cn

Abstract
Seismic facies analysis is of great significance for the detection of residual oil in a sand-shale interbed reservoir. In this study, we propose to predict spatial distribution of sand thickness over a reservoir, based on seismic facies analysis. The target reservoir is a thin sand-shale interbed layer, and the layer thickness varies between 2 and 10 m. The thickness of sand strata within the reservoir layer appears to have a fragmentary distribution in lateral space. Thin thickness and fragmentary distribution are two factors that cause difficulty in sand thickness prediction. To tackle this problem, this study adopted a three-stage strategy. First, the reservoir over the entire study area was classified into five different lithofacies, following sedimentary microfacies analysis against the characteristics of gamma-ray logging data, and the corresponding seismic responses were meticulously depicted. Then, exploiting these seismic responses, or seismic facies, the spatial distribution of the gamma-ray values was evaluated within the thin sand-shale interbed reservoir. Finally, the spatial distribution of the sand thickness was predicted according to the spatial distribution of the gamma-ray values. The prediction was conducted independently for each seismic facies, rather than in a non-discriminatory manner. Comparing the prediction to the actual evaluation derived from well-logging data demonstrated that the thickness distribution resulting from seismic data has a high accuracy, because of the facies-based analysis.

Keywords: reservoir prediction, sand-shale interbed, sand thickness, sedimentary microfacies, seismic facies

1. Introduction

Seismic characteristics of thin sand-shale interbed reservoirs are of great significance for residual-oil detection, especially for a thin reservoir with a thickness less than 5 m. Widess (1973) defined the thin layer when the thickness was less than a quarter of the wavelength of seismic incident waves propagating through the media. Koefoed (1980) noted that there was a quasi-linear relationship between the thickness of a thin layer and the amplitude of seismic reflection waves.

In reality, however, there are only a few isolated simple thin layers in the subsurface strata, and most probably they are a combination of thin layers or interbeds. Li (1987) noted that the frequency characteristics of seismic waves depended on the combination of sand and shale, and on the hydrocarbon-bearing property of thin layers. Based on an approximate linear relationship between the thickness of thin layers and the amplitude of seismic reflection waves, Su (1988) proposed to make a quantitative evaluation of the thickness of

thin layers and the total thickness of multi-layer reservoirs. Based on the concept of seismic sedimentology, Zeng *et al.* (1998) and Zeng (2001) noted that it was the thin layer that could be distinguished rather than the interfaces within a thin layer.

In practice, the thickness of thin reservoirs can be calculated using the information of amplitude, mean frequency and bandwidth. The calculated thickness is thus more accurate than it is using only the amplitude. Adriansyah & McMechan (2002) used the multivariate regression analysis method to establish the statistical relationship between seismic attributes and reservoir properties, and they used the seismic attributes to predict the stratigraphic properties. Guo *et al.* (2018) extracted seismic amplitude slices to depict the lateral variation of a sand body.

Our prime objective in this paper is to present the prediction of the spatial distribution of the sand thickness within a sand-shale interbed reservoir. The study area is in the middle of an anticlinal structure, and the ultimate aim of this study was the prospection of residual oils in the maturely developed reservoir in the Songliao Basin, northeast China. In this work, the characteristics of the gamma-ray logging data are analysed against the sedimentary microfacies and then the reservoir over the entire study area is classified into five different lithofacies models. Based on the seismic responses, or seismic facies, of these lithofacies models, theoretical gamma-ray values are predicted from seismic impedances. Finally, the spatial distribution of the sand thickness is evaluated quantitatively within the target sand-shale interbed reservoir.

One of the advantages of the methodology that we used in this study is that both gamma-ray prediction and thickness evaluation were conducted independently for each seismic facies, rather than in a non-discriminatory manner. Therefore, the sand thickness distribution resulting from analysing seismic data has a high accuracy, in comparison to the actual evaluation derived from well-logging data.

2. Stratigraphy and lithology of the thin reservoir

The study block lies from the top to the east part of an anticline and is approximately 12 km^2 in size, which is a part of a rectangle with 5.9×3.27 km^2 (figure 1a). The internal structure of the block is relatively flat, with a stratigraphic dip of about 1–2°. The study reservoir is on the eastern part of a northwest-trending normal fault (figure 1b).

Table 1 describes the stratigraphy and lithology of the target reservoir. The Formations G, P and S in the study area were formed under the background of large lacustrine-delta facies from the Turonian–Coniacian stage in the Upper Cretaceous. The Turonian and Coniacian stages are also referred to as the Yao-jia and Qing-shan-kou stages, respectively, by regional geologists. During the deposition process, the chan-
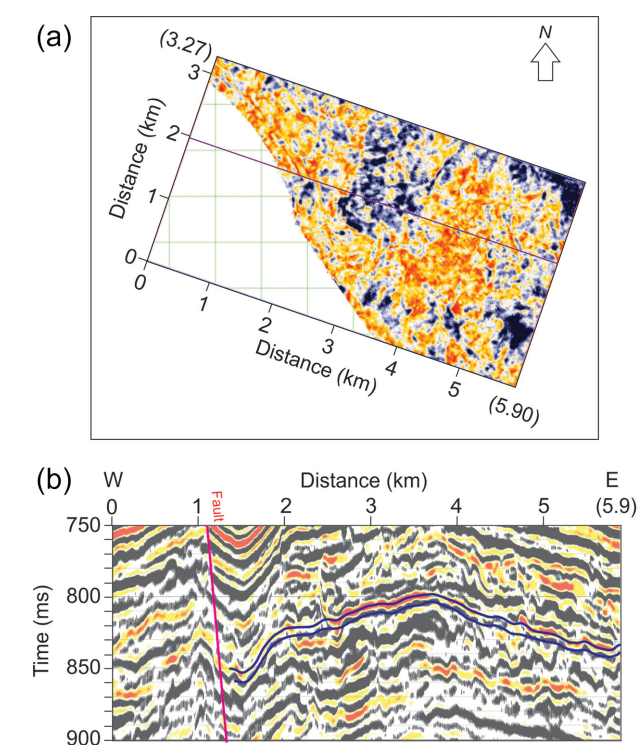
Figure 1. (a) Time slice of 3D seismic data. The study area is approximately 12 km^2. (b) Seismic section (the purple line in a) showing the anticlinal structure of the target reservoir. The two blue curves are the top and the bottom of the reservoir. The study area is on the eastern part of a fault.

nel oscillated frequently, and the energy was strong. Within Formation P, there are multiple oil-producing layers and our study focuses on a thin sand-shale interbed, which is referred to as Layer P_1^2. Two blue curves on the seismic profile are the top and the bottom of the reservoir (figure 1b). During the sedimentary process of P_1^2, this layer developed depositional microfacies such as main channel, abandoned channel and crevasse fan, etc. A channel sand body was developed in a zonal distribution, showing a vertically positive rhythm. When the river moved rapidly laterally, argillaceous and large amounts of sandy sediments were deposited along the flood plain. In addition, the interbed layer formed by the lateral accretion and abandoned channel caused a discontinuity of the sand body locally. The thickness of Layer P_1^2 generally varies between 2 and 10 m.

Layer P_1^2 experienced three sedimentary processes of regression–transgression–regression. By comprehensive analysis of logging data from more than 100 wells in the study block, in conjunction with the characteristics of sedimentary microfacies, the gamma-ray logging data within Layer P_1^2 can be divided into five facies. The corresponding five lithofacies models are determined in the next section. The seismic responses, or seismic facies, are used as the basis for the following evaluation of sand thickness distribution. To our knowledge, this is the first time that this type of analysis procedure has been applied to this study area.

Table 1. Stratigraphic and lithologic properties of the Upper Cretaceous formations. The target oil reservoir is Layer P_1^2 within Formation P.

Series	Stage	Sedimentary facies	Lithology	Oil-producing layer		
				Formation	Layer	
Upper Cretaceous	Coniacian (Yao-jia)	Delta facies	Large segments of dark-grey, grey-green and black-grey mudstone interbedded with silty mudstone.	Formation S	S_1	
					S_2	
			The upper part is the black mudstone and siltstone. The lower part is the interbedding of the dark-grey and green-grey mudstone with the brown-silty mudstone, argillaceous siltstone and siltstone.		S_3	
				Formation P	P_1	P_1^2
	Turonian (Qing-shan-kou)	Deep lacustrine facies	Grey-black and dark-grey mudstone with a thin layer of black ostracoda.		P_2	
				Formation G	G_1	

3. Seismic facies analysis

3.1. Facies analysis of gamma-ray logging data

The logging data are divided into five facies, according to the assemblages of sandstone in three sedimentary stages. Figure 2 displays the selected gamma-ray logging curves of Layer P_1^2, where the black straight lines represent the top and bottom of the target reservoir. In the gamma-ray curves, low amplitudes correspond to the interval of high sandstone content, and high amplitudes represent the interval of shale. The amplitudes of sand and shale are very different.

Facies I shows low values in the gamma-ray logging curve over the entire depth window of the target layer. Its shape is similar to a typical bell or box. It clearly indicates that Layer P_1^2 is a thick sandstone layer.

Facies II shows a serrated shape in the gamma-ray logging curve over the whole of the reservoir, with teeth protruding in the middle of the box. It represents an interbedding configuration of sand-shale-sand. The purple hashed lines divide the layer into three sedimentary stages.

Facies III shows low amplitudes in the gamma-ray logging curve in the middle part. It corresponds to a thin interval of sandstone.

Facies IV shows high amplitudes in the gamma-ray logging curve at the bottom half and low amplitudes at the top half. The abrupt change in between represents an interface between the lithological variation from shale to sand.

Facies V shows low amplitudes in the gamma-ray logging curve at the bottom half and high amplitudes at the top half.

It represents the lithological variation from the sand to the shale.

3.2. Lithofacies models

Analysing the sedimentary microfacies, five lithofacies models (figure 2), corresponding to the five logging facies noted previously, can be drawn as follows.

Lithofacies-model I depicts a large set of sandstones in the course of sedimentation. This deposition represents a main-channel sedimentary microfacies. The set of sandstones has a good stability, and within the sandstone deposition there is a relatively low shale content. The background stratum is mudstone on the top and beneath the bottom.

Lithofacies-model II depicts deposited sandstone, mudstone and sandstone from the bottom to the top. This deposition reflects the process of hydrodynamic variation from strong to weak and to strong again, and it has a mainly dispersed distribution along the edge of the channel.

Lithofacies-model III depicts deposited mudstone, sandstone and mudstone from the bottom to the top. The mudstone that was deposited in the earlier stage was partially washed out and partially retained. Then, a thin sandstone was deposited gradually during water regression. In the later stage, mudstone formations began to be deposited because of transgression and a weak hydrodynamic condition. This mud-sand-mud sedimentary structure can be classified as underwater distributary channel microfacies.

Lithofacies-model IV retains a part of the mudstone layer in the early stage and deposited sandstone in the later stage
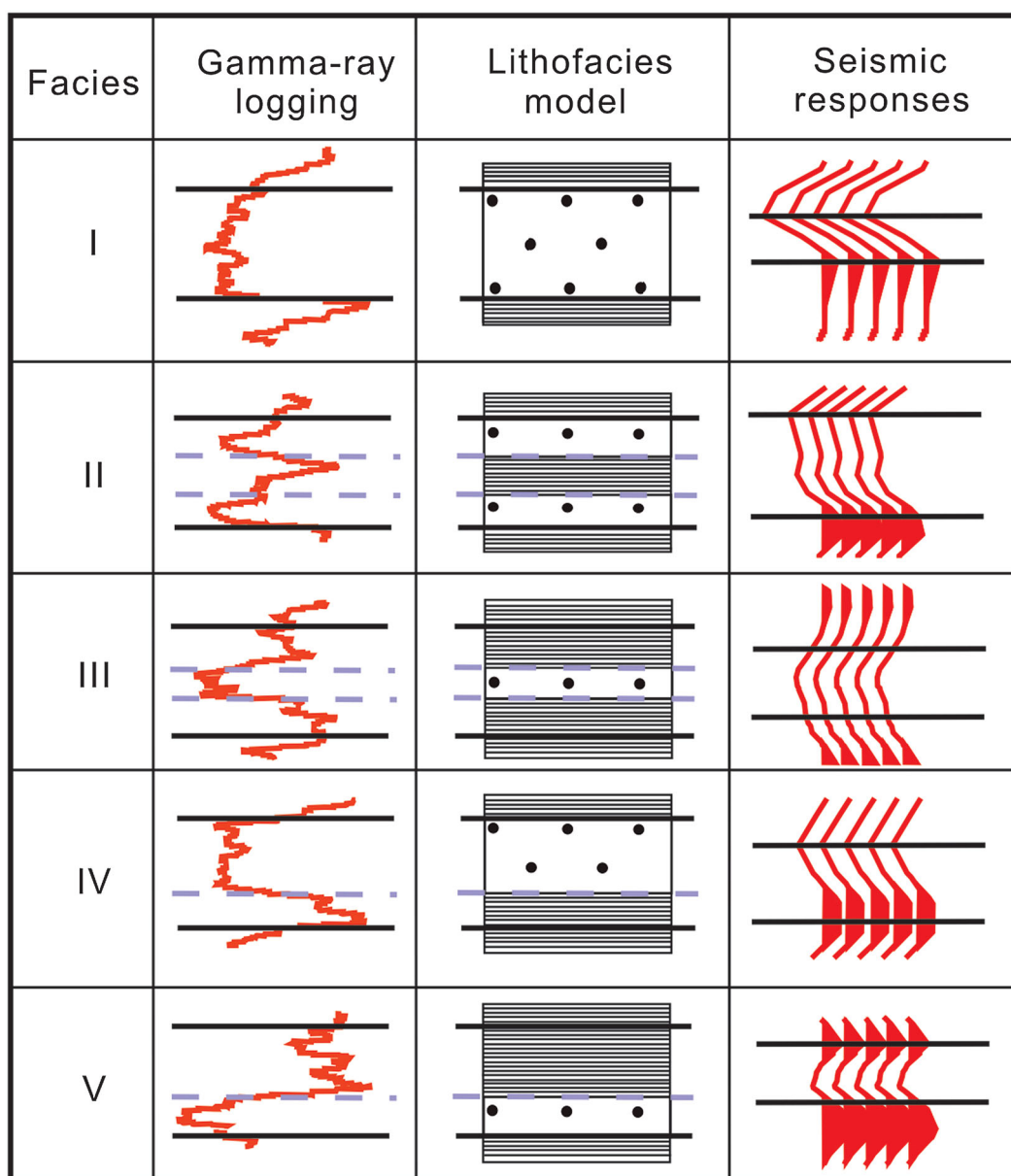
Figure 2. Five microfacies, the corresponding gamma-ray logging curves, lithofacies models and the seismic responses extracted from near-well seismic traces. Two horizontal straight lines are the top and the bottom of the target Layer P_1^2.

on top of the mudstone layer. This sedimentary characteristic reflects the process of hydrodynamic variation from weak to strong, and it represents the sedimentary microfacies of either an underwater distributary channel or an underwater crevasse fan.

Lithofacies-model V depicts the development of a scouring surface in the bottom half and deposited mudstone on the top. This sedimentary characteristic represents sedimentary microfacies of either an underwater abandoned channel or an underwater distributary channel.

Table 2 lists the physical parameters of the five lithofacies models. These parameters are measured from logging data of sample wells. The velocity is measured from sonic logging,

not from seismic data. The velocity of sandstones is lower than the velocity of mudstones, while the density of sandstones is also lower than the density of mudstones. Therefore, the seismic impedance of sandstone is obviously lower than the impedance of mudstones (Yan & Han 2018).

3.3. Seismic facies

Seismic facies, or seismic responses, of five lithofacies models within Layer P_1^2 (figure 2) have obvious differences in the characteristics of composited waveforms. Seismic facies analysis has been widely applied in reservoir geophysics (Liu & Wang 2017; Song *et al.* 2017; Liu *et al.* 2018; Yin *et al.* 2018).

Table 2. Physical parameters of five lithofacies models. These parameters are measured from sample wells.

Facies	Lithology	Thickness (m)	Velocity (m s^{-1})	Density (g cm^{-3})
I	Mudstone		3030.3–3225.8	2.10–2.35
	Sandstone	6–10	2702.7–3125.0	1.90–2.10
	Mudstone		2985.1–3225.8	2.10–2.35
II	Mudstone		2985.1–3225.8	1.80–2.00
	Sandstone	1–5	2631.6–2857.1	1.95–2.10
	Mudstone	0.1–4	3030.3–3125.0	2.20–2.30
	Sandstone	1–5	2597.4–2857.1	1.95–2.10
	Mudstone		2898.6–3125.0	1.85–2.00
III	Mudstone		2985.1–3205.1	2.25–2.35
	Mudstone	1–4	3030.3–3333.3	2.20–2.35
	Sandstone	2–4	2739.7–2985.1	1.90–2.05
	Mudstone	1–4	2898.6–3076.9	2.20–2.30
	Mudstone		2857.1–3125.0	2.23–2.33
IV	Mudstone		2941.2–3174.6	2.30–2.40
	Sandstone	2–6	2631.6–2857.1	2.05–2.20
	Mudstone	1–6	2898.6–3846.2	2.35–2.45
	Mudstone		2941.2–3125.0	2.25–2.35
V	Mudstone		3030.3–3333.3	2.00–2.05
	Mudstone	1–5	2941.2–3448.3	2.30–2.40
	Sandstone	1–5	2666.7–2985.1	2.00–2.20
	Mudstone		3076.9–3333.3	2.00–2.03

The seismic data have been processed using resolution enhancement by seismic inverse-Q filtering (Wang 2002, 2006). Therefore, the dominant frequency of seismic data is as high as around 70 Hz. Seismic waveforms at well locations are taken as the seismic responses of lithofacies models. These waveforms appear in a generalized form, rather than as an idealized Ricker wavelet (Wang 2015). It is simply the result of the superposition of seismic wavelets that are reflected from different interfaces between layers with different thicknesses. In the seismic responses, two horizontal straight lines correspond to the top and the bottom of Layer $P_1{}^2$ (figure 2).

For Facies I, the seismic reflection coefficient at the top of the lithofacies model is negative, while the reflection coefficient at the bottom of the lithofacies model is positive. Because of its large thickness (6–10 m, listed in Table 2), the trough and peak of the waveforms are clearly preserved.

For Facies II, the existence of a thin mudstone interbed affects the waveform that appears in Facies I. The seismic response of Facies II is a composited waveform, in which the top and bottom reflections of the mudstone interbed cannot be separated to make each one independent of the other.

For Facies III, the seismic response of the thin sandstone interbed appears as an interference to the seismic response of the mudstone background. The waveform pattern does show a trough, but does not accompany any immediate peak, either on the top of or beneath the trough.

For Facies IV, the top of the seismic response shows a trough that is similar to the top of the seismic response of Facies I. However, the bottom of the seismic response appears to be a shifted stack of two peaks, instead of a single peak in the seismic response of Facies I.

For Facies V, in which a thin segment of sand body is in the bottom half of the layer, the trough of the waveform corresponds to the top of this sand body and the peak of the waveform corresponds to the bottom of this sand body and the bottom of Layer $P_1{}^2$. The peak of the waveform has a strong amplitude, due to a high impedance difference between the sand body and the surrounding rock outside Layer $P_1{}^2$.

Seismic facies are the basic data for reservoir prediction, and different seismic waveforms correspond to different reservoir characteristics. When applying these five seismic facies to cross-correlate each seismic trace individually, a spatial distribution of seismic facies in Layer $P_1{}^2$ is produced, as shown in figure 3. In the study area, facies I, IV and V are the dominant facies. Facies I shown in orangey red represents the main-channel sedimentary microfacies. Facies IV in purple represents an underwater distributary channel and an underwater crevasse fan sedimentary microfacies. Facies V in turquoise represents an underwater abandoned channel and an underwater distributary channel sedimentary microfacies. Facies II and III are randomly scattered in the facies distribution map. Facies II (in yellow) represents the edge of a river channel, and facies III (in green) represents an underwater distributary channel sedimentary microfacies.
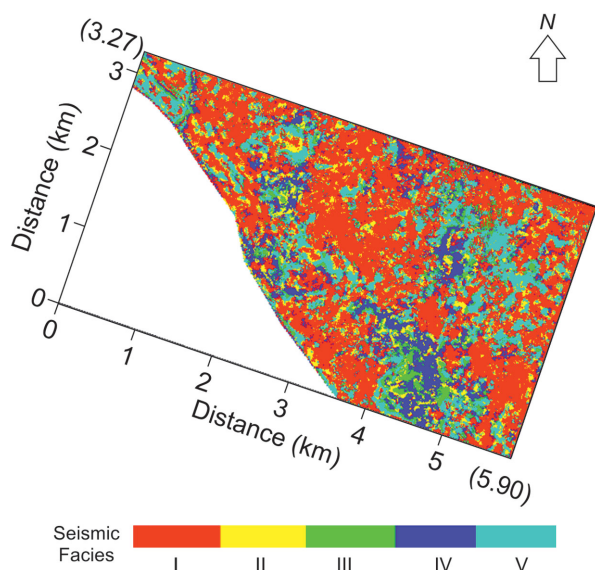
Figure 3. Spatial distribution of seismic facies of Layer $P_1{}^2$. Five facies represented by orangey red, yellow, green, purple and turquoise, respectively, are: (I) the main-channel sedimentary microfacies, (II) the edge of river channel, (III) underwater distributary channel sedimentary microfacies, (IV) underwater distributary channel and underwater crevasse fan sedimentary microfacies and (V) underwater abandoned channel and underwater distributary channel sedimentary microfacies.

4. Prediction of sand thickness distribution

For the prediction of sand thickness distribution, relationships among seismic impedance, the gamma-ray value and thickness of the sand body need to be established.

4.1. The relationship between the gamma-ray value and seismic impedance

The relationship between the gamma-ray values in sample wells and seismic impedances nearby is established by using linear regression on the cross-plots (figure 4). The linear regressions for the five facies are given as per the following:

$$
\begin{aligned}
\gamma &= -518.200 + 0.10100z, \\
\gamma &= -102.134 + 0.03063z, \\
\gamma &= -104.650 + 0.03075z, \qquad (1) \\
\gamma &= -116.875 + 0.03125z, \\
\gamma &= -223.435 + 0.05005z,
\end{aligned}
$$

where z represents seismic impedance, and γ is the gamma-ray value. The correlate coefficients for facies I-V are 0.52, 0.51, 0.90, 0.67 and 0.69, respectively. Note that the correlate coefficient for facies III might be too optimistic since there are only a few samples available.

If using all sample wells together, and not using sample wells according to different seismic facies, the cross-plot (figure 5a) shows that the correlation coefficient between the gamma-ray data and seismic impedance data is 0.41.

Note that samples used in figure 5a are the sum of all samples used in figure 4. Obviously, the correlation coefficients based on samples of any individual facies (figure 4) are higher in value than the correlation coefficient when using all samples in a non-discriminatory manner (figure 5a).

In this study, the consideration of seismic facies has significantly improved the accuracy of the predicted gamma-ray values. In figure 5b, the horizontal axis shows the well numbers that are arbitrarily assigned, and the vertical axis shows the relative error between the theoretically predicted gamma-ray value and the actual gamma-ray logging value of a sample well. In this case study, 58 wells were selected as sample wells from more than 100 wells that were analysed. The red dots denote the relative errors for the prediction using the relationships for five seismic facies separately. The black dots are the relative errors of predictions using the relationship that was established from all sample wells together. Obviously, all of the black dots are higher in value than the red dots. The relative errors of predicted gamma-ray values after dividing seismic facies are mostly less than 10%. Therefore, consideration of seismic facies can improve the accuracy of the following reservoir characterization of thin sand-shale interbeds.

4.2. The relationship between the sand thickness and the gamma-ray value

The lithology within Layer $P_1{}^2$ consists of mainly mudstone and siltstone. Given that gamma-ray logging data are a sensitive parameter to distinguish sandstone and mudstone, the sand thickness of each facies can be estimated statistically from the gamma-ray logging values of sample wells. The estimation can be divided into three steps: (i) an average gamma-ray value of sandstone and mudstone is calculated over a target segment of gamma-ray logging data; (ii) sandstone is determined at a depth if the gamma-ray value is below the average value and (iii) the thicknesses of sandstone are summed vertically to produce the total thickness.

Then, the empirical relationships between the average gamma-ray values and the thickness of the sand body within the reservoir are established for five facies, respectively (figure 6). They are produced by using linear regression over the cross-plots at the positions of sample wells. The empirical relationships for the five facies are given as per the following:

$$
\begin{aligned}
H &= 25.23134 - 0.26144\gamma, \\
H &= 25.15034 - 0.24887\gamma, \\
H &= 213.59467 - 2.45798\gamma, \qquad (2) \\
H &= 50.7605 - 0.56002\gamma, \\
H &= 49.21971 - 0.46315\gamma,
\end{aligned}
$$

where H is the thickness of the sand body. Note that the empirical relationship for facies III is not reliable, since there are only three samples available for linear regression.
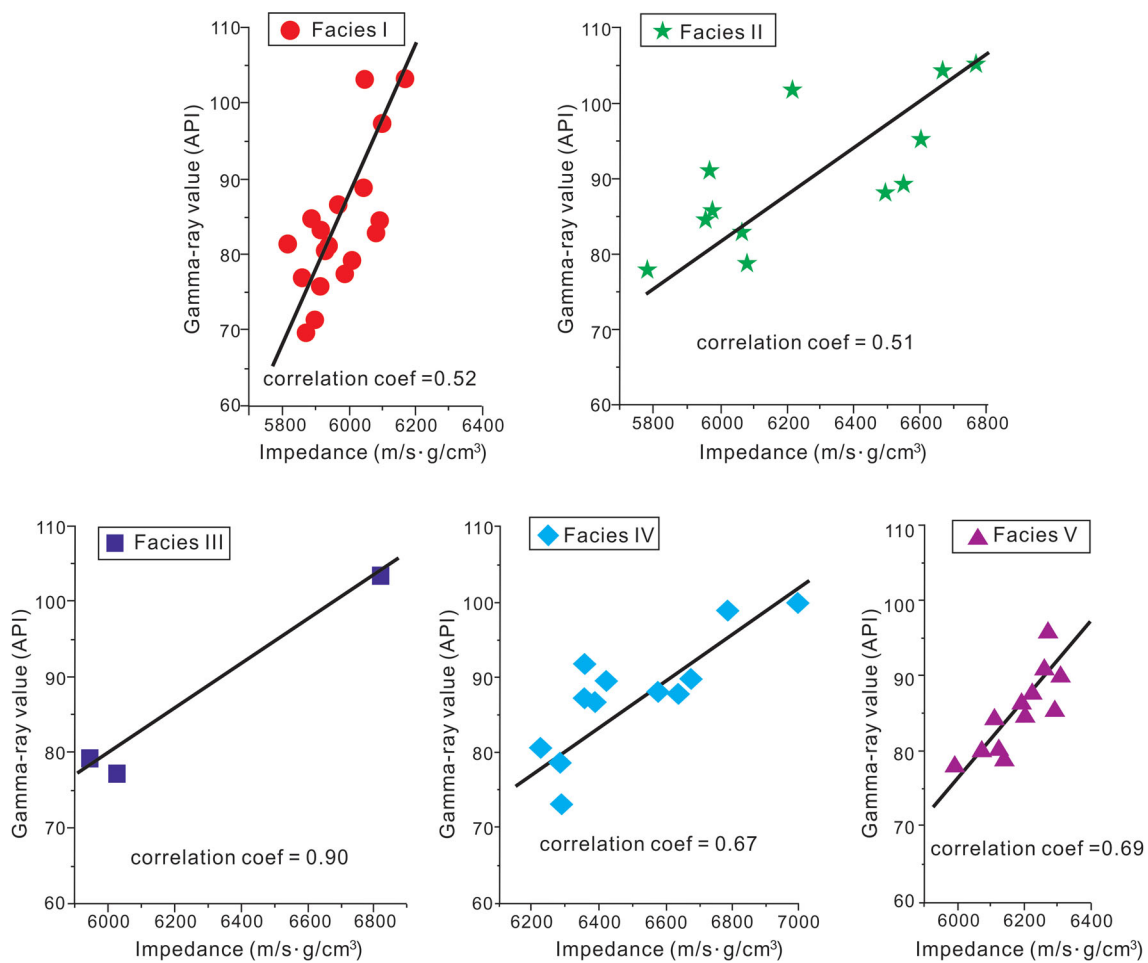
Figure 4. Cross-plots between the gamma-ray values and seismic impedances for seismic facies I, II, III, IV and V.

4.3. *Distribution of the sand thickness*

The previous subsections established the relationship between seismic impedances and gamma-ray values and the relationship between gamma-ray values and the thickness of the sand body within the target reservoir. These relationships were established for each seismic facies separately. Applying these relationships, the thickness of the sand body within Layer P_1^2 can be predicted.

Seismic inversion was implemented to obtain seismic impedance data. A logging-constrained sparse spike inversion method was adopted (Debeye & van Riel 1990; Wang 2016; Alebouyeh & Chehrazi 2018; Liu & Wang 2020). Figure 7a is the inverted seismic impedance. The impedance is an average value over the depth window of each individual seismic trace.

When applying the first group of relationships corresponding to individual facies, the average gamma-ray value at each trace position can be evaluated and the result is shown in figure 7b. Then, the average gamma-ray values are converted to the sand thicknesses. Merging these individual thickness maps into a single map creates the distribution of the sand

thickness of Layer P_1^2 over the study area, as shown in figure 7c.

Three distribution maps in figure 7 show high correlations because of the linear relationships that were used in the predictions. When comparing the results to the amplitude slice (figure 1a), the (anti-)correlation is not that strong, since the strength of seismic impedance is not directly related to the amplitude of seismic waveforms.

Figure 8 validates the thickness prediction, in comparison with the actual thickness of the sand body, within 481 wells over the entire study area. Regarding the test positions, 31.4% have relative errors less than 10%, 60.1% have relative errors less than 20%, 86.3% have relative errors less than 30% and 96.5% have relative errors less than 35%. These relative errors reflect the high accuracy of the sand thickness prediction.

Although we have established the relationship between the gamma-ray value and seismic impedance and the relationship between the sand thickness and the gamma-ray value, both relationships obtained by linear regression are subject to further refinement using, for instance, a bivariate non-linear regression method. Nevertheless, these linear relationships will be reliable references for the investigation
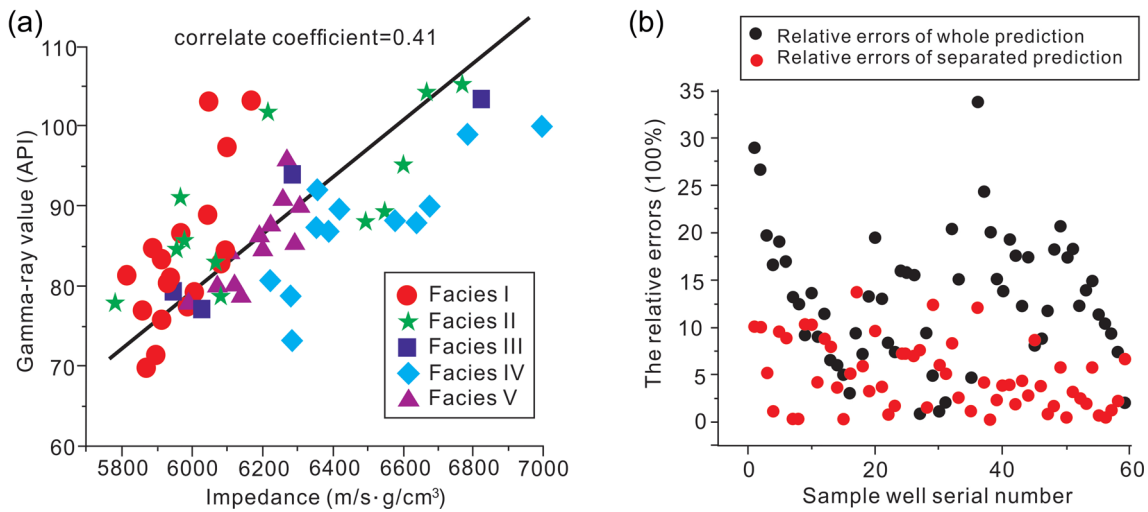
Figure 5. (a) Cross-plot between the gamma-ray values and seismic impedances of all wells. Note the samples in (a) are the sum of samples in figure 4. (b) Gamma-ray relative error of whole prediction and separated seismic facies prediction at Layer P_1^2.
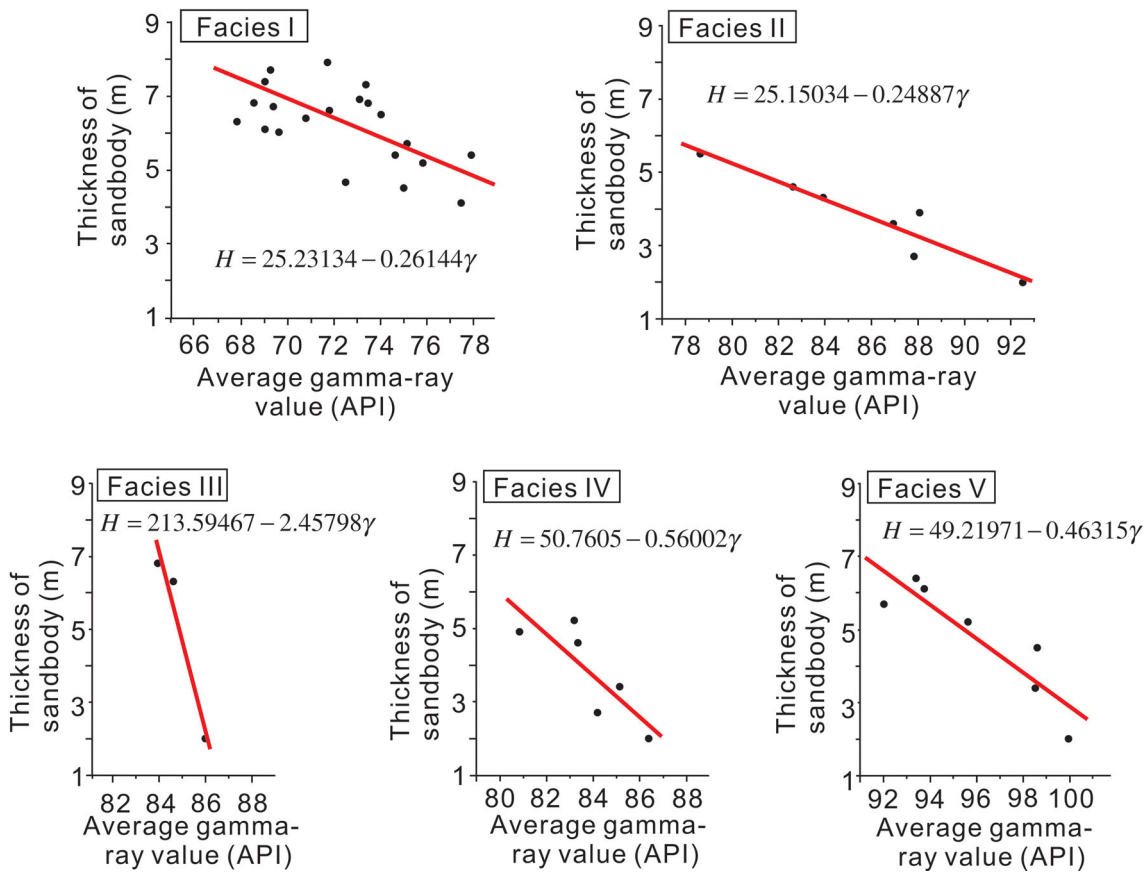
Figure 6. Relationship between the average gamma-ray value and the thickness of sand body within Layer P_1^2.

of multivariate relationships between the sand thickness and multiple geophysical attributes that include the gamma-ray value and seismic impedance. For transforming multiple attributes to the sand thickness, an artificial neural network algorithm might be more effective than the sequential interpretation presented in this study (Wang 2012; Farfour *et al.* 2015; Abdulaziz *et al.* 2019).

5. Conclusion

We have analysed well-logging data against the local stratigraphic and lithologic information. Based on the characteristics of gamma-ray logging data, we have constructed five lithofacies models that represent different combinations of sedimentary microfacies such as main river channel,
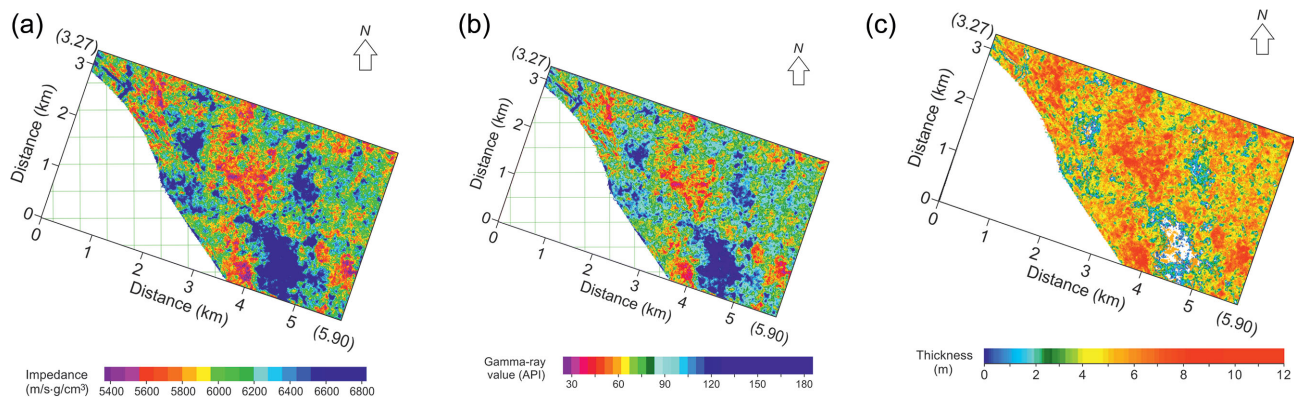
Figure 7. (a) Spatial distribution of inverted seismic impedance within Layer P_1^2. (b) Spatial distribution of predicted gamma-ray values within Layer P_1^2. (c) Spatial distribution of the sand thickness within Layer P_1^2.
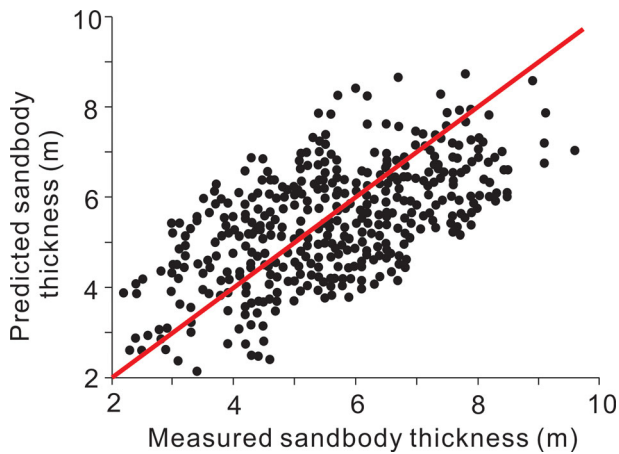
Figure 8. Validation of sand thickness prediction within Layer P_1^2. The horizontal axis is the actual sand thickness measured from well-logging data, and the vertical axis is the predicted sand thickness evaluated from seismic impedance data.

abandoned river channel, crevasse fan, etc. Correlating with the seismic responses of these models, we have predicted the distribution of seismic facies of the target reservoir over the study area.

We have successfully predicted the spatial distribution of sand thickness within the target reservoir, by exploiting the relationship between the gamma-ray logging data at sample wells and seismic impedances for five seismic facies, and the relationship between the average gamma-ray value and the thickness of the sand body within the reservoir. Because these relationships are evaluated for each seismic facies independently rather than in a non-discriminatory manner, we have obtained the prediction of the sand thickness with high accuracy, if comparing the prediction result from seismic data to the actual evaluation from the gamma-ray logging data.

Acknowledgements

References

Abdulaziz, A.M., Mahdi, H.A. & Sayyouh, M.H., 2019. Prediction of reservoir quality using well logs and seismic attributes analysis with an artificial neural network: a case study from Farrud Reservoir, Al-Ghani Field, Libya, *Journal of Applied Geophysics*, **161**, 239–254.

Adriansyah, A. & McMechan, G.A., 2002. Analysis and interpretation of seismic data from thin reservoirs: Northwest Java basin, Indonesia, *Geophysics*, **67**, 14–26.

Alebouyeh, M. & Chehrazi, A., 2018. Application of extended elastic impedance (EEI) inversion to reservoir from non-reservoir discrimination of Ghar reservoir in one Iranian oil field within Persian Gulf, *Journal of Geophysics and Engineering*, **15**, 1204–1213.

Debeye, H.W.J. & van Riel, P., 1990. Lp-norm deconvolution, *Geophysical Prospecting*, **38**, 381–403.

Farfour, M., Yoon, W.J. & Kim, J., 2015. Seismic attributes and acoustic impedance inversion in interpretation of complex hydrocarbon reservoirs, *Journal of Applied Geophysics*, **114**, 68–80.

Guo, C.X., Guo, S.W. & Zhu, W.F., 2018. Research and application of fluvial sand-shale thin interbedding prediction method, *Geophysical & Geochemical Exploration*, **42**, 169–174 (in Chinese).

Koefoed, O., 1980. The linear properties of thin layers, with an application to synthetic seismograms over coal seams, *Geophysics*, **45**, 1254–1268.

Li, Q.Z., 1987. Frequency and amplitude characteristics of oil and gas bearing sand layers, *Oil Geophysical Prospecting*, **1987**, 1–23 (in Chinese).

Liu, J. & Wang, Y., 2020. Seismic simultaneous inversion using a multi-damped subspace method, *Geophysics*, **85**, R1–R10.

Liu, X., Li, J., Chen, X., Guo, K., Li, C., Zhou, L. & Cheng, J., 2018. Stochastic inversion of facies and reservoir properties based on multi-point geostatistics, *Journal of Geophysics and Engineering*, **15**, 2455–2468.

Liu, Y. & Wang, Y., 2017. Seismic characterization of a carbonate reservoir in Tarim Basin, *Geophysics*, **82**, B177–B188.

Song, C., Liu, Z., Cai, H., Wang, Y., Li, X. & Hu, G., 2017. Unsupervised seismic facies analysis with spatial constraints using regularized fuzzy c-means, *Journal of Geophysics and Engineering*, **14**, 1535–1543.

Su, S.F., 1988. Thin-reservoir reflection and the quantitative interpretation method, *Oil Geophysical Prospecting*, **23**, 387–402 (in Chinese).

Wang, Y., 2002. A stable and efficient approach of inverse Q filtering, *Geophysics*, **67**, 657–663.

Wang, Y., 2006. Inverse *Q*-filter for seismic resolution enhancement, *Geophysics*, **71**, V51–V60.

Wang, Y., 2012. Reservoir characterization based on seismic spectral variations, *Geophysics*, **77**, M89–M95.

Wang, Y., 2015. Generalized seismic wavelets, *Geophysical Journal International*, **203**, 1172–1178.

Wang, Y., 2016. *Seismic Inversion, Theory and Applications*. Wiley Blackwell, Oxford.

Widess, M.B., 1973. How thin is a thin bed? *Geophysics*, **38**, 1176–1180.

Yan, F. & Han, D.H., 2018. Application of the power mean to modelling the elastic properties of reservoir rocks, *Journal of Geophysics and Engineering*, **15**, 2686–2694.

Yin, S., Jia, Q. & Ding, W., 2018. 3D palaeotectonic stress field simulations and fracture prediction for marine-continental transitional facies forming a tight-sandstone reservoir in a highly deformed area, *Journal of Geophysics and Engineering*, **15**, 1214–1230.

Zeng, H.L., 2001. From seismic stratigraphy to seismic sedimentology: a sensible transition, *AAPG Bulletin*, **85**, 413–420.

Zeng, H.L., Backus, M.M., Barrow, K.T. & Tyler, N., 1998. Stratal slicing, part I: realistic 3-D seismic model, *Geophysics*, **63**, 502–513.